Fully Wireless Collaborative Beamforming Using A Three-Element Coherent Distributed Phased Array

Jason M. Merlo
Electrical and Computer Engineering
Michigan State University
East Lansing, MI, USA
merlojas@msu.edu

Naim Shandi
Electrical and Computer Engineering
Michigan State University
East Lansing, MI, USA
shandina@msu.edu

Matthew Dula
Electrical and Computer Engineering
Michigan State University
East Lansing, MI, USA
dulamatt@msu.edu

Ahona Bhattacharyya
Electrical and Computer Engineering
Michigan State University
East Lansing, MI, USA
bhatta67@msu.edu

Jeffrey A. Nanzer
Electrical and Computer Engineering
Michigan State University
East Lansing, MI, USA
nanzer@msu.edu

***Abstract*—In this work we experimentally demonstrate a wirelessly coordinated three-element coherent distributed phased array performing beamforming and beam steering to a target in the far-field over 17 m at a carrier frequency of 1.05 GHz. We build on our previous work utilizing a high accuracy two-way time transfer (TWTT) technique for inter-node time synchronization and ranging and an analog continuous two-tone frequency transfer technique to perform syntonization by moving to a fully wireless architecture, without the need for external reference signals such as global navigation satellite system (GNSS)-derived pulse-per-second (PPS), including a distributed computing system architecture, and the use of fully wireless communication links between nodes. Finally, we perform a far-field beamforming experiment with beam steering to a receiver 17 m away at a carrier frequency of 1.05 GHz and demonstrate a beamforming coherent gain of 0.95 (9.32 dB) with a beamforming inter-element timing accuracy of below 60 ps.**

***Index Terms*—distributed antenna arrays, distributed collaborative beamforming, distributed phased arrays, wireless sensor network, wireless synchronization.**

I. Introduction

Recently, interest in the development of wireless coherent distributed phased antenna arrays, shown conceptually in Fig. 1, has been growing due to their applicability in a variety of next-generation technologies ranging from adaptive aperture space-based communication networks [1, TX05.2.6] [2] to satellite and unmanned aerial vehicle-based cellular network infrastructure for 6G communication networks [3], [4], and distributed sensing networks [5]. Interest in such systems is motivated by several benefits over traditional monolithic arrays, namely: the ability to adapt to changing operational and environmental conditions, robustness against node failures, and improved transmit power scaling as N^2 since each node provides its own power source [6]. However, in order to achieve the level of coherence necessary to make the distributed array architecture viable, timing synchronization, frequency syntonization, and phase alignment all must be achieved to a fraction of the radio frequency (RF) carrier wavelength [6]–[8].

979-8-3503-9214-2/24/$31.00 ©2024 IEEE. This work was supported by the Office of Naval Research under grant #N00014-20-1-2389.

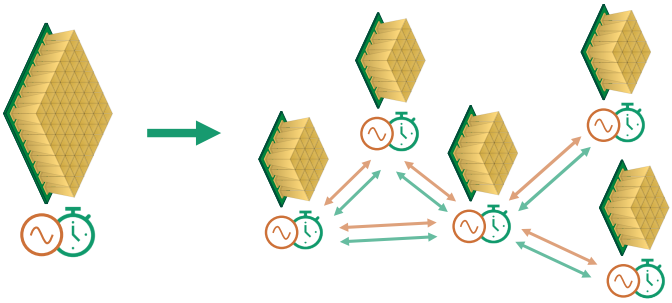

Fig. 1. Distributed phased array concept. A single monolithic phased antenna array may be broken into smaller sub-arrays, or individual elements. The primary challenge is ensuring tight coordination of time, frequency, and phase at all distributed elements.

The topic of wireless distributed collaborative beamforming has been previously explored extensively in terms of array design considerations [9]–[12] and coordination techniques [9], [13]–[24]. Many of these earlier works focused primarily on understanding the feasibility of the technique [9], [13] and implementation of closed-loop techniques, which require feedback from a collaborative beamforming receiver node [14], [15], [25] with impressive experimental results [16] spurring further interest in this area. More recent studies have addressed concerns of energy efficiency in distributed beamforming networks [17]. Recent experimental works have demonstrated collaborative distributed beamforming without feedback from a cooperative receiver [18], [19], [21]–[24], [26]; however, none have demonstrated fully wireless, distributed phased array beamforming with digital timing synchronization at a fraction of the RF carrier level, without the need for external time or frequency references, such as global navigation

satellite system (GNSS).

In this work, we demonstrate a three-element distributed aperture phased array performing fully wireless coordination in time, frequency, and phase, with online inter-node range estimation for beam steering. We improve upon our previous works by:

- Introducing a multi-stage time refinement process with an independent TCP/IP-based initial coarse time alignment/acquisition scheme coordinated over Wi-Fi, eliminating the need for GNSS-derived pulse-per-second (PPS)
- Introducing a distributed computing model to allow each node to perform independent computation and communicate wirelessly via Wi-Fi
- Improving the joint time-range estimation epoch from $\sim$100 ms down to $\sim$10 µs, greatly improving the resilience to ambient motion in the environment
- Including a third beamforming element to further evaluate the scaling of the system to multiple nodes

To evaluate the system, we demonstrate collaborative beamforming and beam steering of both orthogonal linear frequency modulation (LFM) waveforms, so the performance of each element can be individually studied, as well as coherent pulse trains of amplitude modulated pulses, so that the full coherent gain of the system can be observed as the beam is steered over a range of 45°. We show the system achieves a mean coherent gain at broadside of 0.95 (9.32 dB) and a timing accuracy of below 60 ps enabling predicted binary phase-shift keying (BPSK) beamforming rates of up to 1.6 Gbps, based on prior modeling, while beam steering in a cluttered environment [7].

II. Electrical State Coordination

The principal challenge when distributing a phased array into mobile elements is ensuring proper phasing of each element. To accomplish this, the electrical states of the system must be tightly coordinated in time, frequency, and phase [6], [7], [27].

A. Electrical State Model

The time at any node in the array may be represented using a linear model, which, over short time periods, closely approximates the relative clock drift of crystal oscillators. The time offset at the transmitter (TX) or receiver (RX) at any node n may be asymmetrical and is represented by a function of the global true time t

$$T^{(n)}_{\mathrm{T/R}}(t) = \alpha^{(n)}_{\mathrm{T/R}}(t)t + \delta^{(n)}_{\mathrm{T/R}}(t) + \nu^{(n)}_{\mathrm{T/R}}(t) \tag{1}$$

where α is the relative frequency scale, δ is a time-varying bias term, which includes initial system time offsets as well as any time-varying delays through the RF system (such as temperature-varying group delays through, e.g., amplifiers), and ν is a zero-mean noise term. The subscript $\mathrm{TX/RX}$ is shortened to $\mathrm{T/R}$ for compactness of notation. The local oscillator (LO) phase at each RF channel on any node is then given by

$$\phi^{(n)}_{\mathrm{RF,T/R}}(t) = \exp\left\{ j\left[2.0\pi\, f_{\mathrm{RF,T/R}}\, T^{(n)}_{\mathrm{T/R}}(t) \right] + \phi^{(n)}_{0,\mathrm{T/R}} \right\}. \tag{2}$$

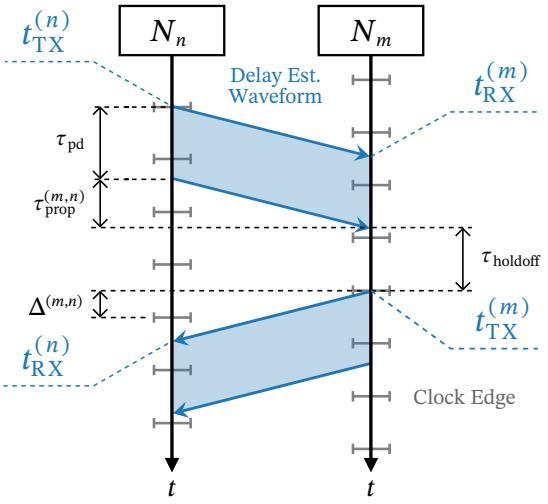

Fig. 2. two-way time transfer (TWTT) diagram showing a single epoch of the time exchange process for two nodes. The transmit and receive times denoted here are the globally referenced times, these timestamps may be converted to the local times at each node using (1). The shaded regions indicate the duration of the pulsed transmission denoted τ_{pd}. The time between node m receiving a message from node n is denoted τ_{holdoff} and is arbitrary so long as the RF channel and system RF properties remain quasi-static.

which describes the RF carrier phase at the transceiver. Thus, to ensure coherent operation of the array we must estimate and correct for α, δ, and ϕ_0 for all nodes; while ϕ_0 should be static and can be calibrated for at relatively infrequent intervals, α and δ vary on the order of seconds due to, e.g., temperature-related changes in component group-delays, and must be constantly estimated and compensated. It should also be noted that to properly steer the beam of the array, the inter-node range must also be estimated.

B. Time and Phase Alignment

In this work, we utilize the high-accuracy two-way time transfer (TWTT) technique described in [28] to determine both the timing offset between elements in the array to a sub-sample level and the inter-node range with sub-centimeter precision [29], [30]. A graphical depiction of this process is shown in Fig. 2. Using the TWTT technique, the time offset between any two nodes in the array may be found from four timestamps representing the time of transmission and reception at each node with reference to its local clock. Using (1) we can represent, e.g., the received timestamp at node m during the kth synchronization epoch with reference to its local clock as $T^{(m)}_{\mathrm{RX}}(t^{(m)}_{\mathrm{RX}}[k])$. Building on this, we can represent the apparent time-of-flight (ToF) between nodes m and n as

$$\tilde{\tau}^{(n\to m)}[k] = T^{(m)}_{\mathrm{RX}}\left(t^{(m)}_{\mathrm{RX}}[k] \right) - T^{(n)}_{\mathrm{TX}}\left(t^{(n)}_{\mathrm{TX}}[k] \right) \tag{3}$$

this being the *apparent* ToF because it is referenced to two different timebases on the transmitting and receiving nodes, respectively. The time offset between nodes can then be found by

$$\Delta^{(m,n)}[k] = \frac{\tilde{\tau}^{(n\to m)}[k] - \tilde{\tau}^{(m\to n)}[k]}{2}. \tag{4}$$

From this, δ at each node may be estimated relative to an arbitrary reference node as $\Delta^{(m,n)} = \delta^{(m)} - \delta^{(n)}$, assuming that α is equal across all nodes. To obtain the true ToF, the apparent ToFs for the kth synchronization epoch in each direction can simply be averaged

$$\tau^{(m,n)}[k] = \frac{\tilde{\tau}^{(n\to m)}[k] + \tilde{\tau}^{(m\to n)}[k]}{2}. \tag{5}$$

From this, the internode range be found by multiplying (5) by the propagation speed in the medium c

$$R^{(m,n)}[k] = c \cdot \tau^{(m,n)}[k]. \tag{6}$$

The inter-node range $R^{(m,n)}$ may then be used for phase compensation for beam steering, assuming initial phase ϕ_0 at each node is calibrated.

It must also be noted that the accuracy of these estimates is critical in ensuring a high level of synchronization. While the transmitted waveform can be estimated to within the clock jitter of the platform by scheduling the transmission to begin on a clock edge at the digital to analog converter, the receive time of arrival is considerably more difficult to estimate as the waveform may arrive at any time between clock edges, as depicted in Fig. 2. To optimize the receive side estimation ability, a two-tone waveform is used because it yields the lowest Cramér-Rao lower bound for time delay estimation for a given bandwidth [31]. Afterwards, a matched filter is performed to determine the coarse time delay estimate to within a single clock cycle of the analog to digital converter; finally, a two-step refinement process using quadratic least-squares (QLS) and a lookup table to compensate for residual bias is used to refine the estimates to sub-sample accuracy [28].

C. Frequency Syntonization

The alignment of frequency, or *syntonization*, is performed using the centralized, two-tone continuous-wave system like those described in [18], [32]. In this system, a two-tone reference frequency is transmitted at an arbitrary carrier frequency with a tone separation equal to the reference frequency used to discipline the LOs on the radio nodes; this compensates for α at all nodes by aligning them with a reference node. The receiver for this system, shown in Fig. 3, operates by first bandpass filtering the input signal at the carrier frequency using a high Q factor filter, then amplifies, and self-mixes the signal with itself, producing a fundamental tone at the beat frequency of the two-tone waveform, which was chosen to be the reference frequency of the system, and higher frequency terms; this signal is simply low-pass filtered to remove the higher harmonics, then amplified to provide the reference frequency to receiving nodes. In this work, the transmitter is realized using a signal generator and the receiver is implemented using discrete analog components.

III. System Configuration

The experimental system configuration consisted of a three-node distributed phased array which was coordinated fully wirelessly in time, frequency, and phase. A system schematic is shown in Fig. 3 and the experimental setup is shown in Fig. 4. Four Ettus Research X310 Universal Software Radio Peripherals were used in this experiment to perform the time and phase coordination, and beamforming operations. Each SDR was run with a base clock rate of 200 MHz and a digital sampling rate of 200 MSa/s and utilized two UBX-160 daughterboards, supporting 160 MHz of instantaneous analog bandwidth. The system operated in a centralized topology with node 0 as the primary node. One SDR on each node was used for time synchronization and ranging on channel 0 and beamforming on channel 1, and node 0 used a second SDR for an auxiliary triggering signal implemented to trigger the receiver. The receiver was a Keysight DSOS8404A oscilloscope which sampled at a rate of 20 GSa/s; channel 1 was used to receive the beamforming waveforms while channel 3 was used for the triggering control and used a high Q factor filter to mitigate unwanted ambient RF signals from triggering the oscilloscope. The beamforming antennas used on the nodes and receiver were 10-dBi L-Com HG72710LP-NF log-periodic antennas and the triggering antennas used were 8-dBi L-Com HG2458-08LP-NF log-periodic antennas.

The primary node was used as the frequency, time, and positional reference. This node contained a Keysight PSG E8267D vector signal generator used as the primary reference frequency which disciplined the LOs of the SDRs on node 0 directly, and the LOs of the secondary nodes via wireless frequency transfer. The reference port of the signal generator was connected to the reference input of SDR 0 to provide the required 10 MHz frequency reference and its RF port was connected to a power combiner to be sent from the joint time-frequency-ranging antennas. From the RF port, the signal generator transmitted a continuous two-tone signal with a tone separation of 10 MHz at a carrier frequency of 4.3 GHz. Two self-mixing frequency locking circuits are connected to the reference input ports on SDRs 2 and 3 to provide the 10 MHz frequency references. The joint time-frequency-ranging antennas used on the secondary nodes were L-Com HG2458-08LP-NF 8-dBi log-periodic antennas; the primary node used a commodity omni-directional dipole antenna.

The system utilized a distributed computing model such that parts of the computation process were performed across separate host computers, one on each node. Nodes 0 and 1 used desktops with Intel i7-8700's while Node 2 used an Intel i7-9700; all three hosts contained 16 GB of DDR4 memory and ran Ubuntu 22.04. The SDRs were connected to the host computers through 10 Gigabit Ethernet (GbE) cables and were controlled using GNU Radio software with custom controller and signal processing blocks written in C++ and Python. To enable network communication of the electrical states and ranging coordination, the primary node host was connected to a Wi-Fi router via 1 GbE while the other two nodes were connected to Wi-Fi modems. The time and phase synchronization (inter-node ranging) were achieved using the TWTT method described in Section II-B and used a pulsed two-tone waveform with pulse duration τ_{pd} of 5 μs and a carrier

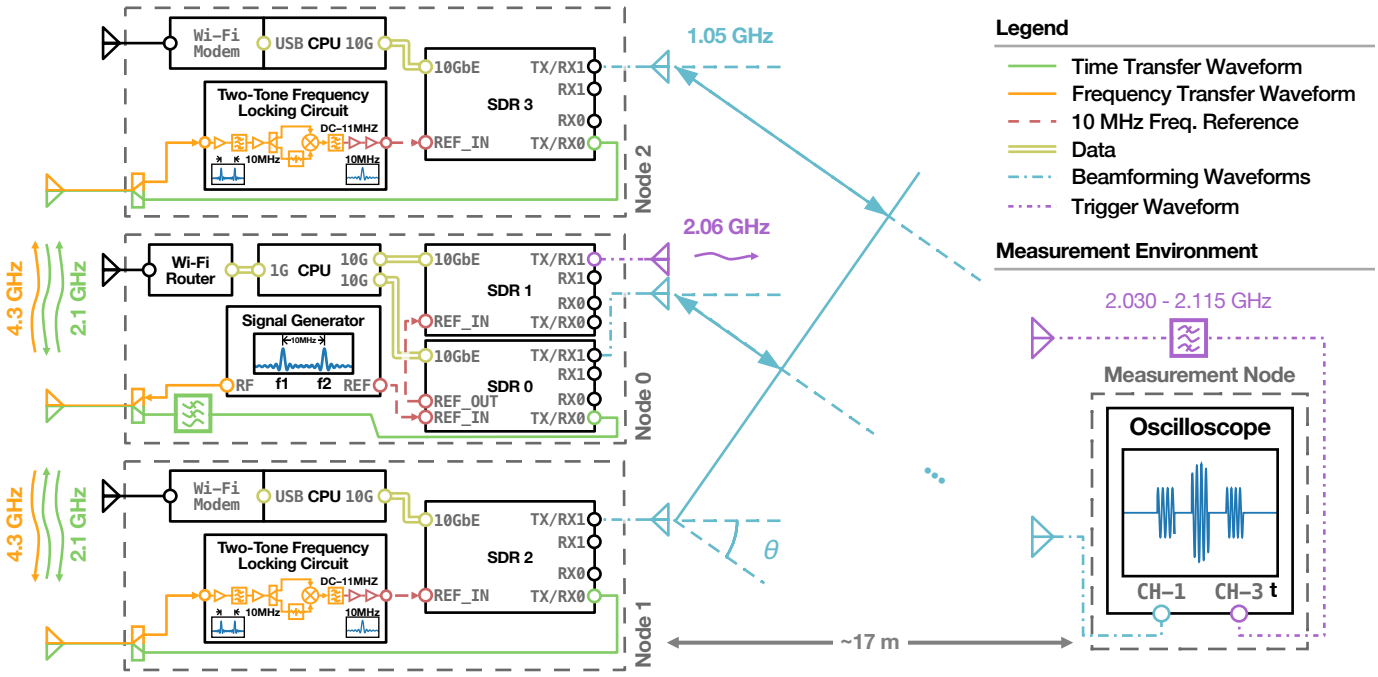

Fig. 3. Distributed array system schematic. Three mobile carts were used to construct the distributed array nodes. Each node contained its own computer and Wi-Fi interface; the primary node hosted a Wi-Fi router while the other nodes used Wi-Fi modems to communicate coordination information with the rest of the array. The primary node also hosted the signal generator which was used as the primary frequency reference; the SDRs on node 0 were disciplined directly by its reference output while the other nodes used two-tone frequency locking circuits to demodulate the two-tone waveform transmitted from the RF port. Time and frequency coordination utilized shared antennas. Beamforming antennas were connected to a separate RF channel on the SDRs. An oscilloscope placed in the far-field was used as a receiver and an auxiliary triggering antenna was used between node 0 and the oscilloscope. A narrow-band filter was placed on the triggering receiver to remove unwanted RF to trigger the oscilloscope only on pulses transmitted from the array, independent of beamforming performance.

Fig. 4. Photograph of the distributed phased array. Antenna masts are placed along the far edge of the carts. On the far side of the mast are 10-dBi log-periodic antennas, on the near side are 8-dBi log-periodic antennas on the secondary nodes while the primary node has an omnidirectional commodity dipole antenna. In front of the array near the ground is the triggering antenna which also used an 8-dBi log-periodic antenna; similar 10-dBi and 8-dBi log-periodic antennas were included on the receiver cart located ∼17 m downrange for receiving beamforming and triggering waveforms, respectively.

frequency of 2.1 GHz. The initial clock alignment process was performed over the network via TCP/IP to an accuracy of ∼10 ms. After the coarse network timing synchronization, the iterative refinement high accuracy synchronization process started at a sample rate of 5 MSa/s, tone separation of 2 MHz, and with a time-domain multiplexing (TDM) window separation of 10 ms; the TDM window separation was then iteratively refined down in geometrically decreasing steps to 5 µs. Once the TDM window is below 1 ms, the sample rate is increased to 200 MSa/s and the tone separation is increased to 40 MHz to reach a fine level of synchronization. A flow chart of this process is included in Fig. 5 and the refinement parameters used in this experiment are provided in Table I. Utilizing this technique, we eliminate the need for external time references such as GNSS-derived PPS entirely.

The three nodes were positioned in a straight line to simplify localization of the nodes to only the inter-node range estimation and each element was separated by 525 mm. The receiver was placed at ∼17 m, approximately at broadside to the array, and beamforming was performed at 1.05 GHz.

IV. Beamforming

To evaluate the overall performance of the system, beamforming was performed to a receiver at a static location while the beam was steered from 0° to 45°. To accomplish this, two

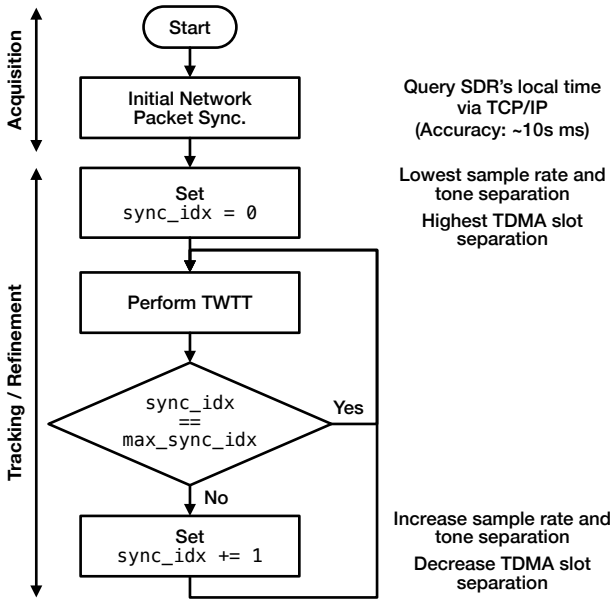

Fig. 5. Time synchronization refinement process flow chart. The system initially obtains a coarse time synchronization by querying the local time on each radio over the network via TCP/IP. Next, TWTT is performed over the network at a low sample rate and tone separation and with a long receive window duration commensurate with the level of synchronization. Each iteration the receive window is decreased and sample rate and tone separation are increased until the desired level of coordination accuracy is achieved. The coordination parameters used in this experiment are shown in Table I.

TABLE I
TIME SYNCHRONIZATION REFINEMENT PARAMETERS

Sync Index	TDMA Slot Separation	Sample Rate	Tone Separation
0	10.0 ms	5 MSa/s	2.0 MHz
1	1.50 ms	5 MSa/s	2.0 MHz
2	223.6 µs	200 MSa/s	40.0 MHz
3	33.4 µs	200 MSa/s	40.0 MHz
4	5.0 µs	200 MSa/s	40.0 MHz

calibration processes were first implemented: inter-node range calibration, and beamforming delay and phase calibration.

The inter-node range calibration step is required to remove the static component of δ which manifests as a static range estimation bias due to RF transmission lines, component group delays, and digital signal processing delays incurred after the waveform is shifted out of the field-programmable gate array (FPGA), which keeps track of the time on the SDR, into the data converters which perform interpolation and decimation. This inter-node range calibration step is accomplished by placing the synchronization antennas at a known baseline separation, computing the ToF based on this known separation, subtracting this value from the estimated ToF, then storing the residual component of the estimated ToF to be used as calibration at runtime

$$\delta_{\mathrm{cal}}^{(m,n)} = \hat{\delta} - d/c \tag{7}$$

where d is the known antenna separation and c is the speed of light in the medium. While this step requires the system to be static so an accurate physical measurement of element positions can be obtained, this is only necessary to be performed once to calibrate out the static signal processing delays, and static delays due to cables and interconnects.

The second calibration step is the beamforming phase calibration. This step is required to estimate $\phi_{0,\mathrm{TX}}$ so that the phases properly align at the desired receiver, as well as to estimate the static delays $\tau_{\mathrm{bf,cal,TX}}$ due to RF channel properties and digital signal processing, similarly to the inter-node range calibration. In this experiment the calibration was performed in the far-field in a pair-wise manner by transmitting orthogonal LFM waveforms from node 0 and one other node; the LFM transmitted at node 0 was a 160 MHz up-chirp while the other nodes transmitted 160 MHz down-chirps in a TDM manner. The waveform was received in the far-field at an oscilloscope and sampled at 20 GSa/s. The inter-arrival delay and phase were estimated using a matched filter and QLS refinement process, similar to the time estimation process described in II-B. Once the calibration parameters were estimated they were simply added to the transmitted beamforming waveforms to ensure proper time and phase alignment in the far field while beam steering. Similarly to the inter-node range calibration, this must only be run once in a static, known configuration to calibrate for the static system delay and phases.

To perform the overall system evaluation the LFM waveforms were used to determine the time of arrival at the receiver while the beam was steered. The phase accuracy was measured by estimating the coherent gain of the system as the beam was steered. The transmitted signals after calibration may be represented by

$$s_{\mathrm{TX}}^{(n)}(t,\theta) = \exp\left\{ j \left[2.0\,\pi\, f_{\mathrm{RF,TX}}\, s_{\mathrm{b}} \left(T_{\mathrm{TX}}^{(n)}(t) - \tau_{\mathrm{bf}}^{(n)}(\theta) \right) - \phi_{\mathrm{bf}}^{(n)}(\theta) \right] \right\} \tag{8}$$

where $s_{\mathrm{b}}(t)$ is the baseband signal to be transmitted from the array, $\tau_{\mathrm{bf}}^{(n)}(\theta) = (R^{(0,n)} - \delta_{\mathrm{cal}}^{(0,n)})/c \, \sin\theta + \tau_{\mathrm{bf,cal}}^{(n)}$, $\phi_{\mathrm{bf}}^{(n)}(\theta) = \phi_0^{(n)} + 2.0\pi\, f_{\mathrm{RF,T/R}}\, \tau_{\mathrm{bf}}^{(n)}(\theta)$, and θ is the beam steering angle.

At each steering angle, three measurements of LFMs followed by the amplitude modulated pulse train were collected sequentially. To estimate the coherent gain G_{c}—the ratio of received signal power to the ideal signal power received at the target if all electrical states were perfectly synchronized—an amplitude modulated pulse train was transmitted, shown in Fig. 6. In this pulse train, the time was divided into seven slots—the first three slots were allocated to each node individually, the following three slots were combinations of two nodes, and the final slot was all three nodes transmitting simultaneously. If all nodes are transmitting coherently, the final pulse magnitude should equal the summation of the magnitude of the first three pulses scaled by the array pattern at the given beam steering angle. The peak amplitudes were estimated by downconverting the waveforms to baseband by

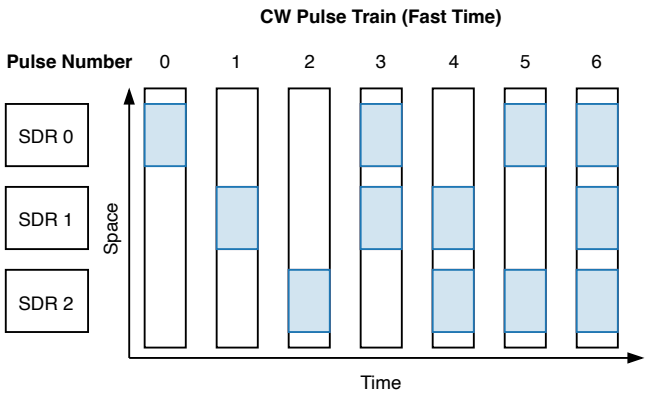

Fig. 6. Coherent gain evaluation modulation pattern. All combinations of SDRs are evaluated. If the time and phase delays are appropriately aligned, the coherent gain of the last pulse (summation of all nodes) will equal that of the first three pulses (each node transmitting individually), scaled by the array pattern for the beam steering angle.

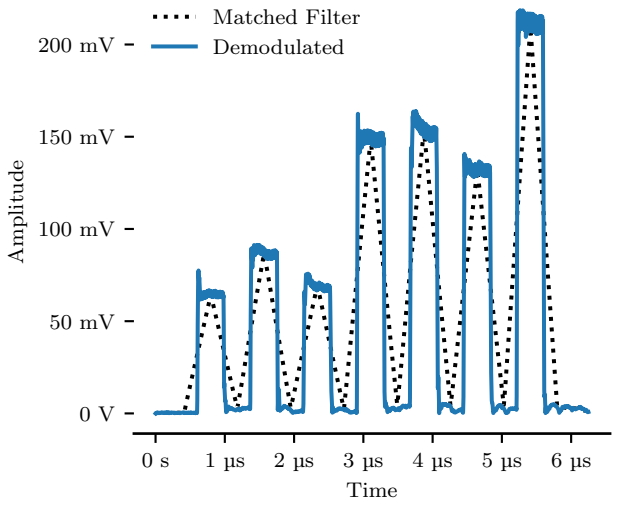

Fig. 7. Measured coherent gain evaluation pulse train. The solid line indicates the filtered and demodulated waveform peak magnitude while the dotted line indicates the matched filter for the pulses. This illustrates the summations of the space-time modulated waveform shown in Fig. 6.

digitally mixing them with the carrier frequency of 1.05 GHz, then matched filtering against the pulse duration of 770 ns. A sample of the coherent gain pulse measurements with the beam steered to broadside is shown in Fig. 7.

V. Measurement Results

The beam steering measurement results are provided in Figs. 8 and 9. Fig. 8 shows the beamforming time delay performance measured at the receiver. The top plot shows the total estimated time delay of the LFM waveforms transmitted from nodes 1 and 2, relative to node 0; the bottom plot shows the deviation from the expected time delay based on the known inter-element spacing. Deviations from this are primarily due to inter-range estimation errors and frequency jitter causing

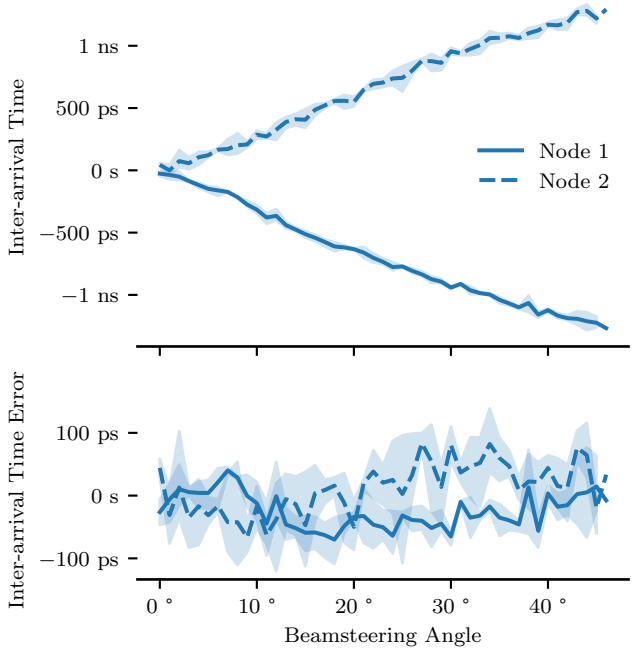

Fig. 8. Estimated inter-arrival times of LFM pulses transmitted from each node, relative to node 0, versus beam steering angle (top). Deviation from expected inter-arrival time based on the geometric time delay for the known antenna baseline (bottom). The traces indicate the mean value while the shaded region indicates the minimum and maximum extents of the collected pulses at each angle.

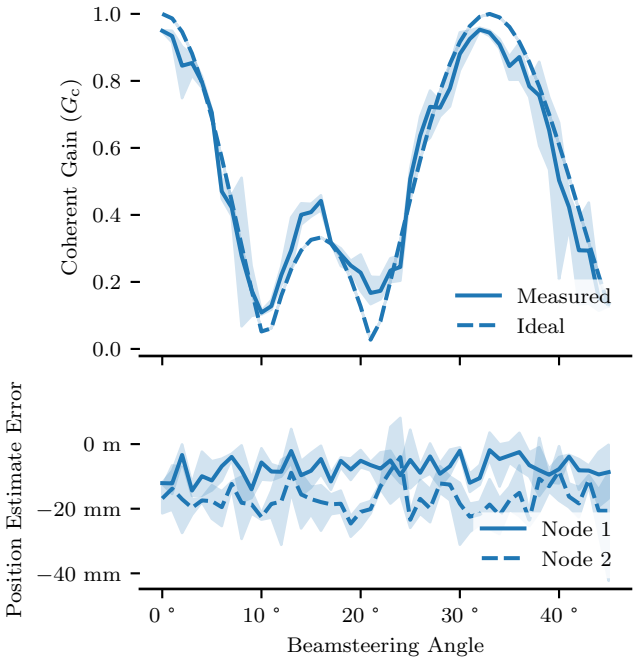

Fig. 9. Estimated coherent gain versus beam steering angle (top). Estimated inter-node position error versus beam steering angle (bottom). The traces indicate the mean value while the shaded region indicates the minimum and maximum extents of the collected pulses at each angle.

distortion of the LFM waveforms. The mean bias across both elements was -6.92 ps with a standard deviation of 50.68 ps. Fig. 9 shows the coherent gain measured at the static receiver as a function of beam steering angle in the top plot and the inter-node position estimation error, relative to node 0, measured at nodes 1 and 2 in the bottom plot. This figure clearly shows the high level of beamforming phase stability indicating an average coherent gain of 0.95, or 9.32 dB for a three-element array, when the beam is steered to broadside. The inter-node ranging accuracy measured at each steering angle is shown in the bottom plot of Fig. 9 which indicates a sub-two-centimeter accuracy during the experiment which yields a coherent gain pattern very close to the expected, ideal antenna pattern as shown in the dashed line in the top plot; significant bias in the inter-node range would manifest as a noticeably increased or decreased beam steering rate than that desired based on whether the ranges were over- or under-estimated, respectively.

VI. Conclusion

In this work we experimentally demonstrate a fully wireless three-element distributed phased array performing collaborative beamforming at 1.05 GHz with beam steering from broadside to 45° over 17 m, without the need for external reference signals such as GNSS-derived PPS signals. The system beam accuracy was shown to be below 60 ps, yielding expected beamforming data rates of up to $\sim$1.6 Gbps while beam steering in a cluttered environment using a BPSK waveform, based on prior studies [6], [7]. These results show significant step towards scaling the system to larger distributed phased arrays.

References

[1] "2020 NASA technology taxonomy," National Aeronautics and Space Administration, Tech. Rep. HQ-E-DAA-TN76545, Jan. 2020.

[2] M. B. Quadrelli, R. Hodges, V. Vilnrotter, S. Bandyopadhyay, F. Tassi, and S. Bevilacqua, "Distributed swarm antenna arrays for deep space applications," in *2019 IEEE Aerospace Conference*, 2019, pp. 1–15.

[3] Z. Xu, G. Chen, R. Fernandez, Y. Gao, and R. Tafazolli, "Enhancement of direct leo satellite-to-smartphone communications by distributed beamforming," *IEEE Transactions on Vehicular Technology*, pp. 1–13, 2024.

[4] G. Sun, J. Li, A. Wang, Q. Wu, Z. Sun, and Y. Liu, "Secure and energy-efficient uav relay communications exploiting collaborative beamforming," *IEEE Transactions on Communications*, vol. 70, no. 8, pp. 5401–5416, 2022.

[5] D. Tagliaferri, M. Rizzi, S. Tebaldini, M. Nicoli, I. Russo, C. Mazzucco, A. V. Monti-Guarnieri, C. M. Prati, and U. Spagnolini, "Cooperative synthetic aperture radar in an urban connected car scenario," in *2021 1st IEEE International Online Symposium on Joint Communications & Sensing (JC&S)*. IEEE, 2021, pp. 1–4.

[6] J. A. Nanzer, S. R. Mghabghab, S. M. Ellison, and A. Schlegel, "Distributed phased arrays: Challenges and recent advances," *IEEE Trans. Microw. Theory Techn.*, vol. 69, no. 11, pp. 4893–4907, 2021.

[7] P. Chatterjee and J. A. Nanzer, "Effects of time alignment errors in coherent distributed radar," in *2018 IEEE Radar Conference (RadarConf18)*, 2018, pp. 0727–0731.

[8] J. A. Nanzer, R. L. Schmid, T. M. Comberiate, and J. E. Hodkin, "Open-loop coherent distributed arrays," *IEEE Trans. Microw. Theory Techn.*, vol. 65, no. 5, pp. 1662–1672, 2017.

[9] H. Ochiai, P. Mitran, H. Poor, and V. Tarokh, "Collaborative beamforming for distributed wireless ad hoc sensor networks," *IEEE Transactions on Signal Processing*, vol. 53, no. 11, pp. 4110–4124, 2005.

[10] K. Buchanan and G. H. Huff, "A stochastic mathematical framework for the analysis of spherically-bound random arrays," *IEEE Transactions on Antennas and Propagation*, vol. 62, no. 6, pp. 3002–3011, 2014.

[11] D. Overturf, K. Buchanan, J. Jensen, C. Flores-Molina, S. Wheeland, and G. H. Huff, "Investigation of beamforming patterns from volumetrically distributed phased arrays," in *MILCOM 2017 - 2017 IEEE Military Communications Conference (MILCOM)*, 2017, pp. 817–822.

[12] A. G. Kanatas, "Spherical random arrays with application to aerial collaborative beamforming," *IEEE Transactions on Antennas and Propagation*, vol. 71, no. 1, pp. 550–562, 2023.

[13] R. Mudumbai, G. Barriac, and U. Madhow, "On the feasibility of distributed beamforming in wireless networks," *IEEE Transactions on Wireless Communications*, vol. 6, no. 5, pp. 1754–1763, 2007.

[14] D. R. Brown III and H. V. Poor, "Time-slotted round-trip carrier synchronization for distributed beamforming," *IEEE Transactions on Signal Processing*, vol. 56, no. 11, pp. 5630–5643, 2008.

[15] M.-O. Pun, D. R. Brown, and H. V. Poor, "Opportunistic collaborative beamforming with one-bit feedback," *IEEE Transactions on Wireless Communications*, vol. 8, no. 5, pp. 2629–2641, 2009.

[16] P. Bidigare, M. Oyarzyn, D. Raeman, D. Chang, D. Cousins, R. O'Donnell, C. Obranovich, and D. R. Brown, "Implementation and demonstration of receiver-coordinated distributed transmit beamforming across an ad-hoc radio network," in *2012 Conference Record of the Forty Sixth Asilomar Conference on Signals, Systems and Computers (ASILOMAR)*, 2012, pp. 222–226.

[17] B. Béjar Haro, S. Zazo, and D. P. Palomar, "Energy efficient collaborative beamforming in wireless sensor networks," *IEEE Transactions on Signal Processing*, vol. 62, no. 2, pp. 496–510, 2014.

[18] O. Abari, H. Rahul, D. Katabi, and M. Pant, "Airshare: Distributed coherent transmission made seamless," in *2015 IEEE Conference on Computer Communications (INFOCOM)*, 2015, pp. 1742–1750.

[19] S. Prager, M. S. Haynes, and M. Moghaddam, "Wireless subnanosecond RF synchronization for distributed ultrawideband software-defined radar networks," *IEEE Trans. Microw. Theory Techn.*, vol. 68, no. 11, pp. 4787–4804, 2020.

[20] H. Ouassal, M. Yan, and J. A. Nanzer, "Decentralized frequency alignment for collaborative beamforming in distributed phased arrays," *IEEE Trans. Wireless Commun.*, vol. 20, no. 10, pp. 6269–6281, 2021.

[21] K. Alemdar, D. Varshney, S. Mohanti, U. Muncuk, and K. Chowdhury, "RFClock: timing, phase and frequency synchronization for distributed wireless networks," in *Proceedings of the 27th Annual International Conference on Mobile Computing and Networking*, 2021, pp. 15–27.

[22] S. R. Mghabghab and J. A. Nanzer, "Microwave ranging via least-squares estimation of spectrally sparse signals in software-defined radio," *IEEE Microw. Wireless Compon. Lett.*, 2021.

[23] J. M. Merlo, A. Schlegel, and J. A. Nanzer, "High accuracy wireless time-frequency transfer for distributed phased array beamforming," in *2023 IEEE/MTT-S International Microwave Symposium - IMS 2023*, 2023, pp. 109–112.

[24] J. M. Merlo and J. A. Nanzer, "Wireless time and phase alignment for wideband beamforming in distributed phased arrays," in *IEEE International Symposium on Antennas and Propagation and USNC-URSI Radio Science Meeting*, Jul. 2023, pp. 365–366.

[25] D. Brown, G. Prince, and J. McNeill, "A method for carrier frequency and phase synchronization of two autonomous cooperative transmitters," in *IEEE 6th Workshop on Signal Processing Advances in Wireless Communications, 2005.*, 2005, pp. 260–264.

[26] H. Ouassal, T. Rocco, M. Yan, and J. A. Nanzer, "Decentralized frequency synchronization in distributed antenna arrays with quantized frequency states and directed communications," *IEEE Trans. Antennas Propag.*, vol. 68, no. 7, pp. 5280–5288, 2020.

[27] J. A. Nanzer and V. C. Chen, "Microwave interferometric and doppler radar measurements of a uav," in *2017 IEEE Radar Conference (RadarConf)*. IEEE, 2017, pp. 1628–1633.

[28] J. M. Merlo, S. R. Mghabghab, and J. A. Nanzer, "Wireless picosecond time synchronization for distributed antenna arrays," *IEEE Transactions on Microwave Theory and Techniques*, vol. 71, no. 4, pp. 1720–1731, Dec. 2022.

[29] N. Shandi, J. M. Merlo, and J. A. Nanzer, "Sub-millimeter ranging accuracy for distributed antenna arrays using two-way time transfer," in *2023 IEEE International Symposium on Antennas and Propagation and USNC-URSI Radio Science Meeting (USNC-URSI)*, 2023, pp. 517–518.

[30] A. Bhattacharyya, J. M. Merlo, and J. A. Nanzer, "A dual-carrier linear-frequency modulated waveform for high-accuracy localization in distributed antenna arrays," in *2023 20th European Radar Conference (EuRAD)*, 2023, pp. 331–334.
[31] J. A. Nanzer and M. D. Sharp, "On the estimation of angle rate in radar," *IEEE Trans. Antennas Propag.*, vol. 65, no. 3, pp. 1339–1348, 2017.
[32] S. R. Mghabghab and J. A. Nanzer, "Open-loop distributed beamforming using wireless frequency synchronization," *IEEE Trans. Microw. Theory Techn.*, vol. 69, no. 1, pp. 896–905, 2021.